Journal of
Applied Physics

RESEARCH ARTICLE | JULY 18 2022

Off-axis Raman spectroscopy for nanoscale stress metrology

Zoheb Khan; Thomas Nuytten; Paola Favia; ... et. al

Journal of Applied Physics 132, 035104 (2022)
https://doi.org/10.1063/5.0100602

View Online
Export Citation
CrossMark

Articles You May Be Interested In

Anisotropic stress in narrow sGe fin field-effect transistor channels measured using nano-focused Raman spectroscopy

APL Mater (January 2018)

Metrology of image placement

AIP Conference Proceedings (November 1998)

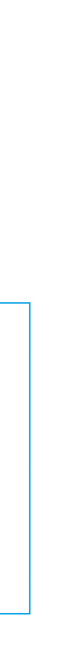

Downloaded from http://pubs.aip.org/aip/jap/article-pdf/doi/10.1063/5.0100602/16510500/035104_1_online.pdf

Time to get excited.
Lock-in Amplifiers – from DC to 8.5 GHz
Find out more
Zurich Instruments

AIP Publishing

Journal of Applied Physics | ARTICLE | scitation.org/journal/jap

Off-axis Raman spectroscopy for nanoscale stress metrology

Cite as: J. Appl. Phys. **132**, 035104 (2022); doi: 10.1063/5.0100602
Submitted: 25 May 2022 · Accepted: 23 June 2022 ·
Published Online: 18 July 2022

Zoheb Khan,[1,2,a)] Thomas Nuytten,[1] Paola Favia,[1] Claudia Fleischmann,[1,2] Ingrid De Wolf,[1,3] and Wilfried Vandervorst[1,2]

AFFILIATIONS

[1]imec, Kapeldreef 75, 3001, Leuven, Belgium
[2]Quantum Solid-State Physics Group, KU Leuven, 3001, Leuven, Belgium
[3]Department of Materials Engineering, KU Leuven, 3001, Leuven, Belgium

[a)]**Author to whom correspondence should be addressed:** zoheb.khan@imec.be

ABSTRACT

Raman spectroscopy is an effective tool for stress and compositional metrology in the semiconductor industry. However, its application toward decoupling a complex stress state in semiconductor materials requires the use of liquid immersion lenses that are process line incompatible. In this work, a practical design concept for off-axis Raman spectroscopy is presented. By tilting the incident light away from the normal incident axis, forbidden Raman modes can be accessed allowing determination of the in-plane stress tensor in semiconductor materials. Furthermore, we benchmark off-axis Raman spectroscopy against oil-immersion Raman spectroscopy for stress characterization in 20 nm-wide strained Ge fin field-effect transistor channels. We demonstrate that off-axis Raman allows anisotropic stress metrology without reliance on liquid immersion lenses, highlighting its viability in the process line. The stress state is validated through nanobeam diffraction measurements.

Published under an exclusive license by AIP Publishing. https://doi.org/10.1063/5.0100602

I. INTRODUCTION

Strain engineering continues to drive the performance in modern three-dimensional transistor architectures. By enabling improvements in carrier mobility, it allows pushing the scaling limits and boosts electrical performance.[1] Naturally, accurately probing strain/stress in nanoscale volumes is an important objective for metrology and crucial for research and development. At the same time, a nondestructive and fast technique that can conform with the requirements of the process line is critical for efficient and economical manufacturing. Currently, quantitative strain measurements in sub-20 nm technology nodes rely on scanning transmission electron microscope (STEM)-based techniques. Typically, strain is measured by either nanobeam diffraction (NBD),[2] geometrical phase analysis,[3] or precession electron diffraction approaches.[4] However, STEM techniques are destructive, time-consuming, and require specific sample preparation that notoriously induces strain relaxation.[4] Alternatively, high-resolution x-ray diffraction is a nondestructive technique for the direct assessment of the lattice parameters. However, the current fab-based tools require large spot sizes (>100 μm) and longer measurement times due to limited intensity of x-ray sources.[5] Furthermore, for strain evaluation in thin films and nanostructures, reciprocal space maps have to be acquired, which significantly increases the measurement time.[6] Raman spectroscopy (RS) is a nondestructive light scattering technique that probes lattice vibrations (phonons). When a material is stressed, the vibration frequency of the phonon changes and affects the wavenumber of the associated Raman mode. If the phonon deformation potentials are known, a quantitative relationship between the mechanical stress and Raman peak frequency can be established.[7] This has led to the widespread application of RS for mechanical stress measurements in the semiconductor industry. Regular (on-axis) RS is not able to differentiate the stress in the various axial directions and only provides the stress value for one direction or a convolution of several directions. For RS to be relevant to the semiconductor industry, this drawback needs to be overcome, as many of the devices used (e.g., narrow fins) have at least biaxial stress distributions. By implementing a novel way of performing RS, i.e., off-axis excitation as originally proposed by Loechelt *et al.*,[8] we broaden the application of RS for determining stress in multiple crystal directions in nanoscale devices.

Downloaded from http://pubs.aip.org/aip/jap/article-pdf/doi/10.1063/5.0100602/16510500/035104_1_online.pdf

Published under an exclusive license by AIP Publishing
This article may be downloaded for personal use only. Any other use requires prior permission of the author and AIP Publishing. This article appeared in Zoheb Khan, Thomas Nuytten, Paola Favia, Claudia Fleischmann, Ingrid De Wolf, Wilfried Vandervorst; Off-axis Raman spectroscopy for nanoscale stress metrology. Journal of Applied Physics 21 July 2022; 132 (3): 035104. and may be found at https://doi.org/10.1063/5.0100602

A. The need for off-axis excitation

The Raman scattering intensity (I) of a phonon vibration is given by[9]

$$I = C\sum_j |E_{out}^T R_j E_{in}|^2. \quad (1)$$

Here, C is a constant and R_j is the Raman polarizability tensor for the jth phonon, E_{out} and E_{in} are the outgoing and incoming polarization vectors, respectively (superscript T indicating the transposed vector). The tensors define the selection rules for detection. For the unstressed diamond-type semiconductors like silicon and germanium, the k = 0 Raman-active phonon is triply degenerate with two transverse optical (TO) modes (TO1 and TO2) and one longitudinal optical (LO) mode. Their polarizability tensors and respective phonon polarizations are given by[10]

$$R_1(TO1) = \begin{pmatrix} 0 & 0 & 0 \\ 0 & 0 & d \\ 0 & d & 0 \end{pmatrix},$$

$$R_2(TO2) = \begin{pmatrix} 0 & 0 & d \\ 0 & 0 & 0 \\ d & 0 & 0 \end{pmatrix}, \quad (2)$$

$$R_3(LO) = \begin{pmatrix} 0 & d & 0 \\ d & 0 & 0 \\ 0 & 0 & 0 \end{pmatrix},$$

$$v_1 = \begin{pmatrix} 1 \\ 0 \\ 0 \end{pmatrix}, \ v_2 = \begin{pmatrix} 0 \\ 1 \\ 0 \end{pmatrix}, v_3 = \begin{pmatrix} 0 \\ 0 \\ 1 \end{pmatrix}. \quad (3)$$

In the presence of anisotropic residual stress, the three phonon frequencies depend differently on all stress tensor elements.[7,11] When assuming that all shear stress components are zero, the concurrent detection of LO and TO modes allows to determine the three main stress components. Experimentally, each mode can be probed by controlling the sample orientation and the polarization state of excitation and Raman scattered light. In the conventional backscattering RS, the light is incident normal to the sample surface and scattering is also collected normally. In this configuration, E_{in} is always parallel to the sample surface. When applied to the most relevant case for semiconductors, i.e., scattering from the (001) surface, only the LO phonon can be detected. As the frequency of this LO phonon depends on all stress tensor elements, it is impossible to determine the anisotropic stress distribution. To overcome this, the Raman configuration needs to be changed such that the incident electric field is not strictly parallel to the sample surface and TO as well as LO modes are excited. Several strategies have been explored in this regard, the current standard being the use of high (>1) numerical aperture (NA) objectives.[12] Here the large focusing angle of the lens results in an increased density of photons with wave vector ($\vec{k}_i$) tilted away from the normal direction of the plane. This tilted contribution adds an $E_{in\perp}$ component as illustrated schematically in Fig. 1(a). The technique has been successfully applied for the excitation of forbidden Raman modes toward decoupling the in-plane stress tensor in nanostructures.[13–16] However, such high-NA objective lenses require liquid immersion (oil/water) environments,[17] contaminating the sample and are a clear roadblock to its in-line adoption. To this end, a "dry" alternative is required. While oblique backscattering approaches have been explored,[18,19] the most efficient scattering configuration for detection of the forbidden TO mode is when incident light is tilted away from the normal axis and the scattered light is collected normally [Fig. 1(b)]. For p-polarized incident light, the $E_{in\perp}$ amplitude responsible for the TO mode excitation scales with the incidence angle (Θ_i). Furthermore, the absorption of the incident radiation maximizes at the materials' Brewster angle, thereby increasing the scattered signal.[20] This so-called

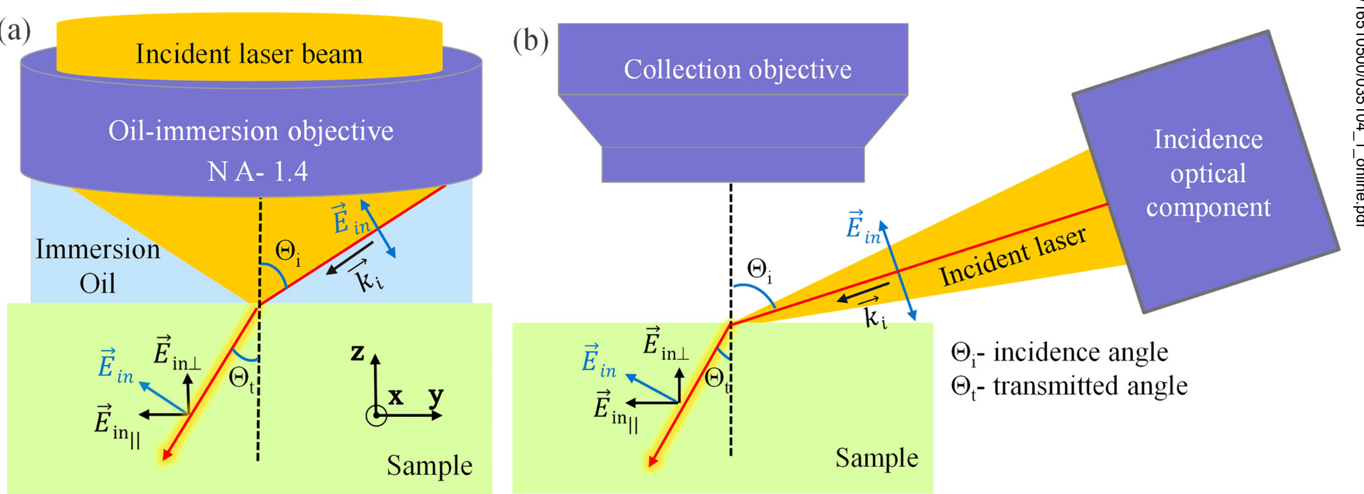

FIG. 1. A schematic comparison of (a) oil-immersion Raman spectroscopy (OIR) and (b) off-axis Raman spectroscopy (FCOR).

Downloaded from http://pubs.aip.org/aip/jap/article-pdf/doi/10.1063/5.0100602/16510500/035104_1_online.pdf

Published under an exclusive license by AIP Publishing

"off-axis Raman scattering" geometry has been applied in the field of RS before.[21,22] In the context of stress metrology, it was first implemented by Loechelt *et al.* and was used to determine the stress tensor in strained Si wafers.[23] Whereas successful as a first demonstrator, their approach and instrumentation did not allow to reach the spatial resolution presently required. Indeed, the conventional approach of splitting the incidence and collection optics with long working distance optical lenses does degrade the spatial resolution. At the same time, it is susceptible to aberrations and presents a technical challenge, making its routine use and implementation problematic. In this work, we overcome these limitations by exploring a simplified, modular approach to off-axis Raman based on an optical fiber-coupled excitation setup, termed FCOR.

II. MATERIALS AND METHODS

A. Analysis techniques

1. Off-axis Raman spectroscopy (FCOR)

A modular setup was realized that can be integrated with any commercial Raman spectrometer; in this case, we used a Labram HR EVO from Horiba scientific. The schematic is shown in Fig. 2(a). It comprises a linearly polarized 633 nm He-Ne laser source coupled to a polarization-maintaining optical fiber (OF). The other end of the OF is coupled to a collimator and focusing lens assembly (NA =0.09) that can focus the beam to a ∼6 μm diameter spot. This collimator is housed on an adjustable flip platform which controls the incidence angle. A manually operated 3D translation stage is fitted with a custom-made platform, which functions as the sample stage. The whole assembly is screwed to a custom-made aluminum breadboard. This breadboard is then placed on the 3D motorized stage of the commercial Raman spectrometer. The scattered radiation is collected by a 50× long working distance objective (NA =0.5) and fed via an appropriate analyzer configuration to the Raman spectrograph equipped with an 1800 line/mm grating. Combining two 3D positioning stages in this way offers the necessary freedom to focus the incident beam at the focal point of the collection objective for a desired location on the sample. All measurements were performed at 60° incidence angle giving an elliptical laser spot with approximate diameters of 6 μm (minor axis) and 12 μm (major axis). The laser power density is maintained below 20 kW/cm^2 to avoid heating-induced peak shifts.[16] The He–Ne laser, in addition to the main lasing line at 633 nm, also produces a collection of non-lasing lines due to additional transitions in the He–Ne system that appear as sharp peaks in the spectrum. These so-called "plasma peaks" are not affected by stress and offer a useful means of calibrating the spectrum against any environmental drifts of the instrument.[24] We note that there are several routes to realizing a dedicated off-axis Raman setup, for instance, with higher NA long working distance objectives and a standalone spectrograph that would potentially offer higher spatial resolution. In order to ensure a modular setup, specific optical and mechanical components were chosen in our case that do not interfere spatially with the commercial spectrometer components. As such, we make a meaningful compromise in spatial resolution, enabling the use of a standard state-of-the-art confocal Raman spectrograph in the detection path.

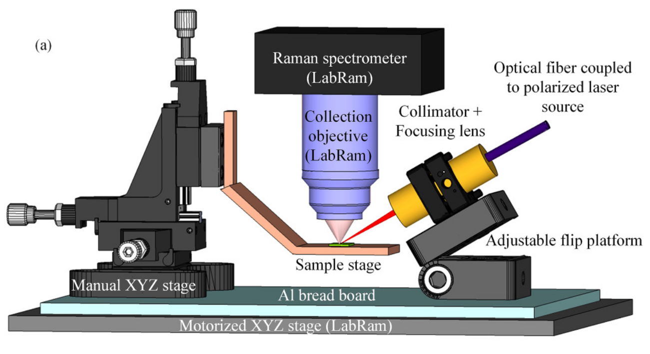

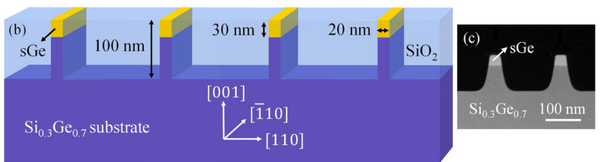

FIG. 2. (a) Schematic-FCOR combined with the commercial spectrometer. (b) Schematic of fin structure exemplifying the layer stack embedded in an SiO_2 matrix. (c) High-angle annular dark-field STEM image of the 20 nm-wide strained Ge (sGe) fin structure.

2. Oil-immersion Raman spectroscopy (OIR)

The OIR measurements are performed with a 633 nm linearly polarized laser source (He–Ne) and an oil-immersion objective with NA = 1.4. The laser spot diameter is about 540 nm theoretically and the spectrograph details are the same as above.

3. Nanobeam diffraction (NBD)

NBD is a TEM-based technique that determines nanoscale variations in the lattice parameters of crystalline materials. Typically, an electron beam is scanned along a region of interest, collecting a series of diffraction patterns. These are compared to a reference diffraction pattern representing the substrate/unstrained region. The local 2D strain is then calculated as the relative lattice mismatch $\Delta d/d$.[25] The measurements here were carried out using an FEI Titan 60-300, equipped with a 20 μm condenser aperture, operating at 300 kV in a μprobe STEM-mode. Under these conditions, an approximate probe beam diameter of 3.5 nm is expected.

B. Sample

1. Raman metrology at the nanoscale

The application of FCOR, as will be shown further, generates insight into the two-dimensional strain distribution and is thus of high relevance for investigating small devices like finFETs. However, in view of their nanoscale dimensions (<20 nm), one is faced with the need for very high spatial resolution, which is not improved by off-axis Raman spectroscopy compared to OIR. Even if nm-resolution could be reached, one will be faced with the important issue of sensitivity. Indeed, the intensity of Raman

Downloaded from http://pubs.aip.org/aip/jap/article-pdf/doi/10.1063/5.0100602/16510500/035104_1_online.pdf

Published under an exclusive license by AIP Publishing

scattering scales with the volume of material under investigation.[26] Hence, the diminishing dimensions of the semiconductor devices represent a growing challenge in terms of detectability applicable to the technique under consideration. One possible solution is to make use of the fact that the Raman intensity also scales with the local electric field at the scattering site. The latter can be increased by exploiting plasmon-based enhancement methods like surface-enhanced Raman spectroscopy (SERS)[27,28] or tip-enhanced Raman spectroscopy (TERS).[29–32] However, the need for sample modification (SERS) and complex instrumentation (TERS) hinders the implementation of such solutions in the process line. A promising alternative to "apparently" achieve the spatial resolution and increase the sensitivity is the ensemble measurement. In this concept, multiple (identical) devices are probed simultaneously thereby providing a large volume of analyzed material and thus sensitivity. Under particular conditions such as Si (or Ge) fins embedded in SiO_2, the RS signal originates almost exclusively from the fin volume thus providing the required spatial resolution. Although the fin region in such a configuration only covers 1%–10% of the total area, the signal intensity is dramatically increased by the geometry-based enhancement of the electromagnetic (EM) field. This arises from the so-called nano focusing effect, which leads to the excitation of an EM field guided mode confined inside the periodic structure.[33] The necessary condition to achieve this is the presence of nm-spaced interfaces of materials, with a strong contrast in dielectric behavior. Based on this effect, Nuytten *et al.* showed that with incident laser light polarized along the length of semiconductor fins, their Raman response enhances dramatically.[34] The concept has widespread applicability in in-line metrology as such device arrangements are universally present in current 3D semiconductor architectures. Moreover, the effect was demonstrated to be present in a variety of materials including semiconductors like Si, Ge, and InGaAs, but can be exploited for dimensional metrology of metal lines as well.[34–36] Based on these observations, we have concentrated our FCOR studies on ensemble-based studies using samples like the one shown in Fig. 2(b).

2. Sample design

The sample consists of strained Ge (sGe) fins enclosed in an SiO_2 matrix. The integration scheme is based on the blanket growth of a 30 nm-thick Ge layer on top of a blanket $Si_{0.3}Ge_{0.7}$ strain relaxed buffer (SRB) on a (001) Si substrate.[37] The blanket Ge is compressively strained due to the lattice misfit. This stack is then patterned into 20 nm-wide, 10 μm-long fins aligned along the $[\bar{1}10]$ crystal direction with a pitch of 180 nm, designed for uniaxial stress along the fin length.[38,39] The space between the fins is refilled with SiO_2 resulting in a periodic grating-like arrangement. This is shown in the schematic [Fig. 2(b)] as well as in the high-angle annular dark-field scanning transmission electron microscopy (HAADF-STEM) image [Fig. 2(c)]. Such fin ensembles extend over a $600 \times 600\,\mu m^2$ region in the die. Since the semiconductor processing is reproducible and thus individual devices are virtually identical, their collective response should be an accurate representation of the individual fin state. Measuring an ensemble of 20 nm fins boosts the signal intensity by over an order of magnitude vs a blanket layer and thus provides the required sensitivity.[33]

III. THEORETICAL BACKGROUND

The presence of strain affects both the frequency of the Raman modes and the polarizability tensor associated to them. The fins in our sample are aligned along the $[\bar{1}10]$ direction, which is the preferred orientation for performance enhancement in strained semiconductor devices. It is convenient here to work with a co-ordinate system $x'y'z'$ defined by [110], $[\bar{1}10]$, and [001] crystallographic directions. Solving for a triaxial stress state with stress in only the principal directions as non-zero, i.e.,

$$\sigma_{x'x'} \neq 0,\ \sigma_{y'y'} \neq 0,\ \sigma_{z'z'} \neq 0. \tag{4}$$

The stress induced Raman peak frequency shifts are given by the equations

$$\begin{aligned}\Delta\omega_{TO1} = \frac{1}{2\omega_0}\Bigg[&\left(\frac{1}{2}(S_{11}+S_{12})(p+q)+qS_{12}+\frac{r}{2}S_{44}\right)\sigma_{x'x'}\\ &+\left(\frac{1}{2}(S_{11}+S_{12})(p+q)+qS_{12}-\frac{r}{2}S_{44}\right)\sigma_{y'y'}\\ &+((p+q)S_{12}+qS_{11})\sigma_{z'z'}\Bigg],\end{aligned} \tag{5a}$$

$$\begin{aligned}\Delta\omega_{TO2} = \frac{1}{2\omega_0}\Bigg[&\left(\frac{1}{2}(S_{11}+S_{12})(p+q)+qS_{12}-\frac{r}{2}S_{44}\right)\sigma_{x'x'}\\ &+\left(\frac{1}{2}(S_{11}+S_{12})(p+q)+qS_{12}+\frac{r}{2}S_{44}\right)\sigma_{y'y'}\\ &+((p+q)S_{12}+qS_{11})\sigma_{z'z'}\Bigg],\end{aligned} \tag{5b}$$

$$\Delta\omega_{LO} = \frac{1}{2\omega_0}[(pS_{12}+q(S_{11}+S_{12}))(\sigma_{x'x'}+\sigma_{y'y'})+(pS_{11}+2qS_{12})\sigma_{z'z'}], \tag{5c}$$

with $\sigma x'x'$, $\sigma y'y'$, and $\sigma z'z'$ representing the stress across the width, along the length and normal to the fin, respectively. ω_0 is the stress-free value for the Raman shift, and the stiffness tensor elements S_{ij} and phonon deformation potentials p, q, and r are material-specific parameters. For Ge,[40,41] $S_{11} = 9.64 \times 10^{-12}\ Pa^{-1}$; $S_{12} = 2.60 \times 10^{-12}\ Pa^{-1}$; $S_{44} = 14.89 \times 10^{-12}\ Pa^{-1}$; $p/\omega_0^2 = 1.45$; $q/\omega_0^2 = 1.95$; $r/\omega_0^2 = 1.1$. The detailed derivation of Eqs. (5a)–(5c) is in Appendix A.

All measurements in this work were performed in the orientation which supports nano-focusing such that a component of E_{in} is polarized along the fin length—$y' = [\bar{1}10]$. Once the off-axis Raman system is added to the Labram spectrometer, E_{in} polarization is fixed. Since the incident radiation is p-polarized and under oblique incidence, it can be resolved into two components within the sample ($E_{in||}$ and $E_{in\perp}$) as shown in Fig. 1(b). While measuring, the finFET sample is oriented in such a way that $E_{in||} = [\bar{1}10]$ and $E_{in\perp} = [001]$. The selection rules determined for this condition are summarized in Table I. E_{in} is fixed while a polarization analyzer is used to select specific E_{out} polarizations and isolate the different

Downloaded from http://pubs.aip.org/aip/jap/article-pdf/doi/10.1063/5.0100602/16510500/035104_1_online.pdf

Published under an exclusive license by AIP Publishing

TABLE I. Polarization selection rules for the TO1, TO2, and LO modes.

Polarization				Visibility		
E_{in}	Parallel to	E_{out}	Parallel to	TO1	TO2	LO
$\bar{1}10$	y′	$\bar{1}10$	y′	…	…	X
001	z′			…	X	…
$\bar{1}10$	y′	110	x′	…	…	…
001	z′			X	…	…

phonon modes. The detailed derivation of the selection rules is included in Appendix B.

From Table I, by selecting E_{out} parallel to x', the TO1 scattering is allowed. This selection is henceforth referred to as the TO-active configuration. On the other hand, selecting E_{out} parallel y′, the LO and TO2 peaks are detectable. Since the refractive index of Ge is high (5.47 for 633 nm radiation[42]) Θ_t will be low, so $E_{in\perp} << E_{in||}$. The relative intensity of the LO peak will expectedly dominate the spectrum masking the TO2 contribution. It is therefore referred to as the LO-active configuration.

IV. RESULTS AND DISCUSSION

Figure 3(a) shows the RS measurement of a 20 nm-wide fin ensemble with FCOR, whereby the overlapping Raman spectra measured under the LO- and TO-active condition are normalized to the Ge peak. The main features are the Rayleigh scattered plasma peak around 286 cm^{-1} coming from the He–Ne laser, a broad feature around 293 cm^{-1} representing the Ge–Ge vibration in the $Si_{0.3}Ge_{0.7}$ SRB and a sharp feature around 305 cm^{-1} representing the strained Ge (sGe) scattering. The sGe peak in the TO-active spectrum is slightly downshifted with a shoulder toward the lower wavenumber side. Due to the imperfect polarization

Downloaded from http://pubs.aip.org/aip/jap/article-pdf/doi/10.1063/5.0100602/16510500/035104_1_online.pdf

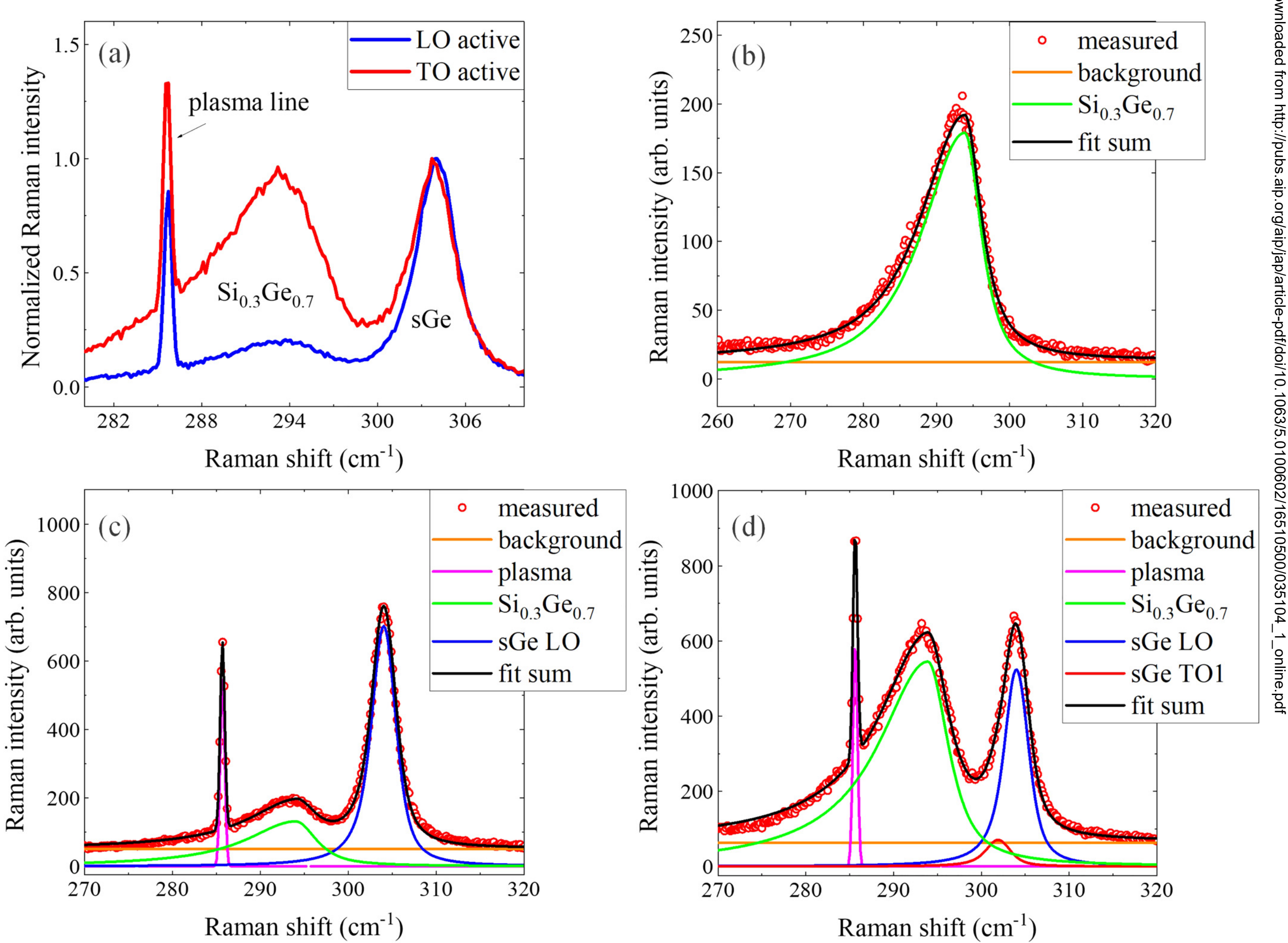

FIG. 3. (a) Normalized Raman spectra with FCOR for 20 nm fins in LO- and TO-active condition overlapped. Fitted spectra, (b) $Si_{0.3}Ge_{0.7}$ substrate, (c) fins LO-active, and (d) fins TO-active.

Published under an exclusive license by AIP Publishing

selectivity of the analyzer and nano-focusing enhancement of $E_{in||}$,[34] it is assumed that the TO-active spectrum is still dominated by the contribution of the LO peak. This implies that the overall TO-active spectrum is still a combination of the $Si_{0.3}Ge_{0.7}$, LO, and TO1 sGe peaks.

Such an overlap requires a systematic approach to the spectral data analysis:

(a) First an exposed $Si_{0.3}Ge_{0.7}$ region from the same wafer is measured and fitted with a constant line for background and an asymmetric pseudo-Voigt function[43] for the Raman response as shown in Fig. 3(b).
(b) Then, the fins are measured in the LO-active condition and the spectrum is fitted with a constant background, while the $Si_{0.3}Ge_{0.7}$ peak width and shape are locked to the substrate measurement.
(c) The sGe peak is best fitted to an asymmetric Voigt shape (confirmed with R^2 analysis). The overall fit matches the measured data very well as seen in Fig. 3(c).
(d) Following this, the TO-active spectrum is fitted [Fig. 3(d)], whereby the parameters of the $Si_{0.3}Ge_{0.7}$ and sGe LO peak (position, width, and shape) are fixed based on the LO spectrum. We also fix the TO peak width and shape to the LO value assuming that any asymmetric broadening is the same for both. The TO peak height and position are free parameters and the variables to the optimization algorithm (Levenberg–Marquardt optimization).[44]
(e) Finally, the peak positions obtained are subtracted from the positions of the Raman peak of a stress-free bulk Ge to calculate $\Delta\omega_{TO1}$ and $\Delta\omega_{LO}$. To account for instrumental/environmental effects, all peak position values are calibrated against the plasma line from the He–Ne laser, itself fitted to a Gaussian shape.

Downloaded from http://pubs.aip.org/aip/jap/article-pdf/doi/10.1063/5.0100602/16510500/035104_1_online.pdf

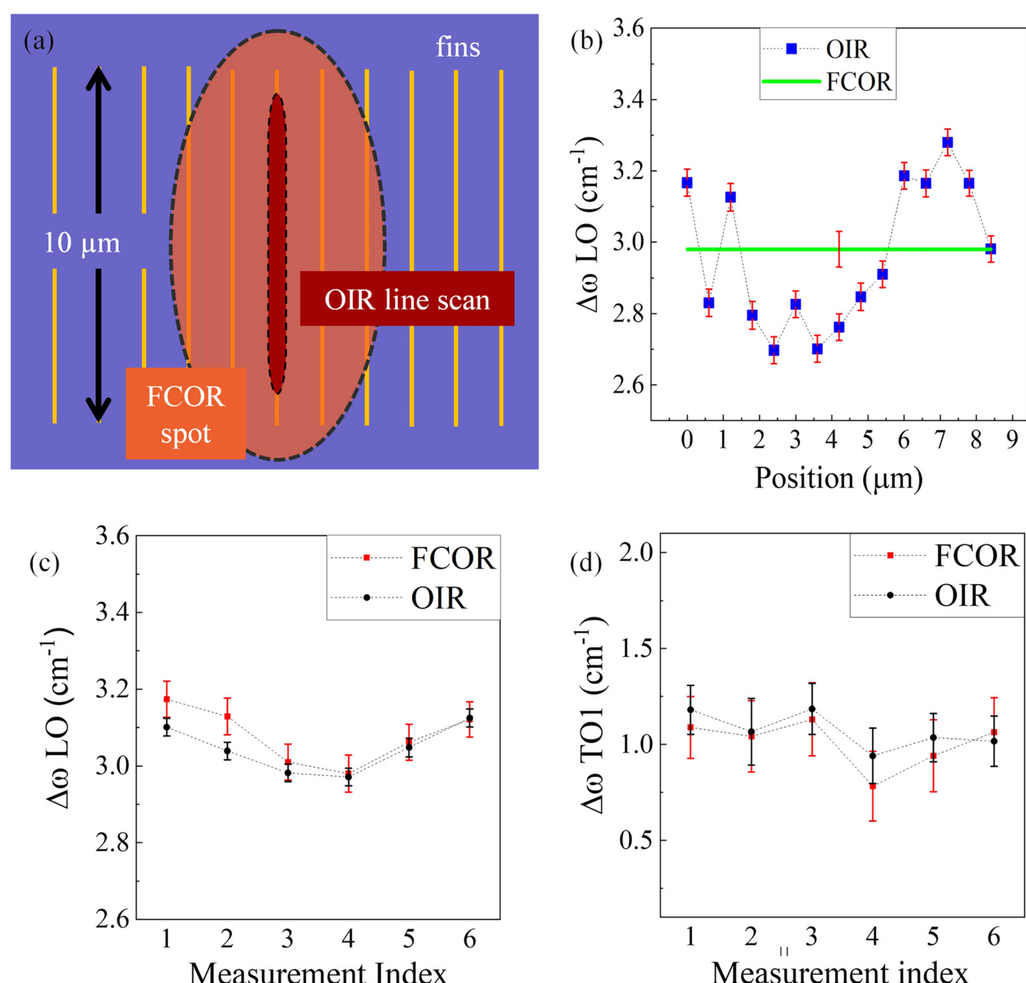

FIG. 4. (a) Schematic comparison of the FCOR and OIR measurement areas. (b) $\Delta\omega_{LO}$ for the OIR line scan and FCOR single spectrum. FCOR single spot vs OIR line scan comparison (c) $\Delta\omega_{LO}$ (d) $\Delta\omega_{TO1}$.

Published under an exclusive license by AIP Publishing

For validation, the stress measurements with the off-axis Raman technique (FCOR) are compared to state-of-the-art oil-immersion Raman spectroscopy (OIR) measurements done in the backscattering configuration. The OIR laser is linearly polarized with $E_{in||}$ also along the fin length. The selection rules are the same as in Table I. We note that in view of the different areas probed by OIR (~0.23 μm^2) and FCOR (~56 μm^2), the entire FCOR illuminated area must be spatially mapped in both LO- and TO-active

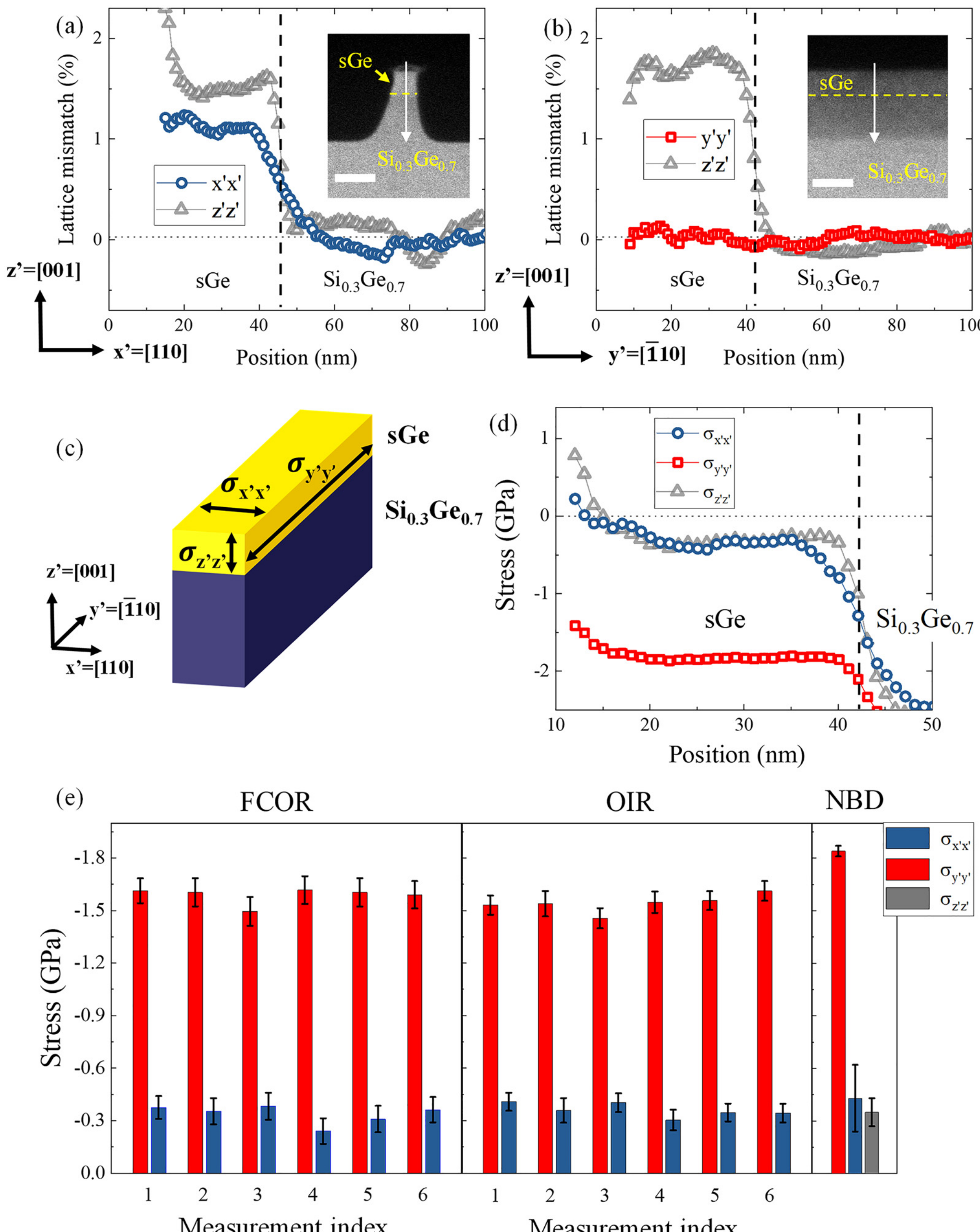

FIG. 5. NBD line profile of lattice mismatch vs $Si_{0.3}Ge_{0.7}$ (a) across the fin lamella (b) along the fin lamella (inset scale bar =50 nm). (c) Schematic description of the finFET (d) Stress distribution in the Ge channel calculated from the cross-sectional measurement of lattice mismatch (valid only in sGe layer). (e) In-plane stress values in the Ge channel region compared across the measurement techniques. (d) is adapted from Nuytten *et al.*, APL Mater. **6**, 058501 (2018); licensed under a Creative Commons Attribution (CC BY) license.

Downloaded from http://pubs.aip.org/aip/jap/article-pdf/doi/10.1063/5.0100602/16510500/035104_1_online.pdf

Published under an exclusive license by AIP Publishing

conditions with OIR to compare the two techniques. However, considering the long measurement times associated with mapping (especially for TO-active condition), OIR line scans were performed at the FCOR measurement spots. A schematic comparison of the measurement areas is shown in Fig. 4(a). The step size of the OIR line scan is maintained at 600 nm (spot size 542 nm) to ensure full coverage and the scan is restricted to the length of the fin. Figure 4(b) plots $\Delta\omega_{LO}$ for such a line scan against the result from a single FCOR spectrum. The error limits shown represent the standard deviation in the peak position obtained after spectrum fitting.[44] A clear variation in the peak positions is noted along the fin length. This variation is attributed to local differences in the stress state within the fin. TEM images taken across the fin cross sections have shown misfit dislocations at the sGe-$Si_{0.3}Ge_{0.7}$ interface. Such dislocations can locally relax the epitaxial strain affecting the Raman peak position. Indeed, this result underscores the importance of comparing single FCOR spectra with OIR averages and justifies the asymmetric shape of the sGe peak. Other factors affecting the Raman peak shape include doping,[45,46] laser-induced heating, and geometrical confinement.[47] Since the processing scheme for the fabrication of the sGe fins did not involve a doping step,[39] a doping induced peak broadening is not expected in our results. Furthermore, considering the laser power and the geometrical size of the fins, heating and confinement factors can also be neglected.

Such an FCOR vs OIR comparison is repeated for six different locations in the die. The spectra from an OIR line scan are averaged and fitted with the same fitting routine discussed above. Figures 4(b) and 4(c) compare $\Delta\omega_{LO}$ and $\Delta\omega_{TO1}$ for single FCOR spectra vs the OIR line scan average. The two techniques agree very well across the six measurement spots. To determine the stress state of the fins, we can substitute $\Delta\omega_{LO}$ and $\Delta\omega_{TO1}$ values into Eqs. (5a) and (5c) which leads to a system of two equations with three variables ($\sigma_{x'x'}$, $\sigma_{y'y'}$ and $\sigma_{z'z'}$). Here, it is typical to assume a biaxial stress state with $\sigma_{z'z'} = 0$, to simplify the equations. However, in this case, we benefit from nanobeam diffraction (NBD) measurements done on a similar structure for the validation of the Raman results. Since NBD analysis is done on the projection through the thickness of the sample, it is not possible to deduce the strain parallel to the electron propagation direction. As a result, both across [inset Fig. 5(a)] and along (longitudinal) the fin [inset Fig. 5(b)] TEM cross section lamellae are needed to evaluate strain along the three principal directions x', y', and z'. The vertical line profiles in Figs. 5(a) and 5(b) plot the relative lattice mismatch in the specimen against the lattice constant of the $Si_{0.3}Ge_{0.7}$ substrate. The dashed line marks the interface between sGe and $Si_{0.3}Ge_{0.7}$. The e-beam is scanned from the top of the fin to the SRB as indicated by the arrow. Analyzing the line profiles reveals that the sGe conforms with the $Si_{0.3}Ge_{0.7}$ lattice constant in the y' direction but deviates in the x' direction suggesting a relaxation of the misfit strain in x'. This lattice mismatch is used to calculate the material strain (with respect to bulk Ge) and finally the stress in the three principal directions, plotted in Fig. 5(d). Since photons of the wavelength used for the current Raman analysis can penetrate the full sGe layer, the Raman response is an average value for the whole sGe depth. Hence, for comparison, we calculate the average stress values from the NBD results. The stress is most pronounced in the direction along the channel $\sigma_{y'y'}$=−1.84 GPa, with a small, nonzero

TABLE II. Average stress values in the Ge channel. FCOR and OIR are averaged over six measurement spots and uncertainties represent the standard deviation. NBD values are averaged over Ge depth for a single measurement and error values are the standard deviation obtained over the averaged region.

Technique	$\sigma_{x'x'}$ (GPa) across fin width	$\sigma_{y'y'}$ (GPa) along fin length
FCOR	−0.34 ± 0.05	−1.59 ± 0.05
OIR	−0.36 ± 0.04	−1.54 ± 0.05
NBD	−0.43 ± 0.19	−1.84 ± 0.03

compressive component present both across $\sigma_{x'x'}$=−0.43 GPa, and in the vertical direction $\sigma_{z'z'}$=−0.35 GPa. Then, by substituting $\sigma_{zz'}$ = −0.35 GPa, in Eqs. (5a) and (5c) $\sigma_{x'x'}$ and $\sigma_{y'y'}$ are determined for the Raman results of Figs. 4(c) and 4(d). The results are plotted in Fig. 5(e) and their averages indicated in Table II.

Expectedly from the peak position comparison, the results for the two Raman techniques agree within the uncertainties. At the same time, the mostly uniaxial trend is compatible with the NBD result. This mostly uniaxial stress state is induced from elastic relaxation at the fin edges due to volume expansion into the free space generated by patterning. We note the difference between the two techniques with Raman showing a lower stress state as compared to NBD. This discrepancy is assumed to be a direct consequence of the difference in the probed areas. While Raman results are an average over the length of an ensemble of fins, the values encompass any relaxation due to defects as highlighted in Fig. 4(b). On the other hand, the nanoscale NBD lamellas give a localized result from seemingly defect free regions and expectedly a higher stress state.

V. CONCLUSIONS

In summary, we have implemented an off-axis design concept for Raman spectroscopy. The technique can access the forbidden transverse optical mode necessary for anisotropic stress measurements while remaining fully non-contact. Aided by nano-focusing of the excitation light, the methodology can readily be applied to nanoscale transistor architectures with adequate sensitivity. We evaluate the stress in 20 nm-wide strained Ge channels revealing a mostly uniaxial stress state, cross-validated with nanobeam diffraction. Overcoming the reliance on liquid immersion lenses truly unlocks the nondestructive advantage of the Raman spectroscopy technique for advanced stress metrology in the process line. Moreover, the application of the off-axis configuration extends to applications beyond stress measurements. For instance, gaining access to both LO and TO modes will increase the accuracy of composition measurements in III-V-based devices. Our results highlight the utility of Raman spectroscopy in the current semiconductor metrology landscape.

ACKNOWLEDGMENTS

The authors would like to acknowledge R. Loo, the EPI team, and Logic Program of imec for sample growth, documentation, and assistance.

Downloaded from http://pubs.aip.org/aip/jap/article-pdf/doi/10.1063/5.0100602/16510500/035104_1_online.pdf

Published under an exclusive license by AIP Publishing

AUTHOR DECLARATIONS

Conflict of Interest

The authors have no conflicts to disclose.

Author Contributions

Zoheb Khan: Conceptualization (lead); Data curation (lead); Formal analysis (lead); Investigation (lead); Methodology (lead); Project administration (lead); Validation (lead); Visualization (lead); Writing – original draft (lead); Writing – review and editing (equal). **Thomas Nuytten:** Conceptualization (supporting); Supervision (supporting); Writing – review and editing (equal). **Paola Favia:** Investigation (supporting); Writing – review and editing (supporting). **Claudia Fleischmann:** Supervision (supporting); Writing – review and editing (equal). **Ingrid De Wolf:** Conceptualization (supporting); Supervision (equal); Writing – review and editing (equal). **Wilfried Vandervorst:** Conceptualization (supporting); Supervision (equal); Writing – review and editing (equal).

DATA AVAILABILITY

The data that support the findings of this study are available from the corresponding author upon reasonable request.

APPENDIX A: RELATION BETWEEN RAMAN FREQUENCY AND RESIDUAL STRESS

The effect of strain on frequency can be deduced by solving the secular equation:[7]

$$\begin{vmatrix} p\epsilon_{xx} + q(\epsilon_{yy} + \varepsilon_{zz}) - \lambda_i & 2r\varepsilon_{xy} & 2r\varepsilon_{xz} \\ 2r\varepsilon_{xy} & p\epsilon_{yy} + q(\epsilon_{xx} + \varepsilon_{zz}) - \lambda_i & 2r\varepsilon_{yz} \\ 2r\varepsilon_{xz} & 2r\varepsilon_{yz} & p\epsilon_{zz} + q(\epsilon_{xx} + \varepsilon_{yy}) - \lambda_i \end{vmatrix} = 0, \tag{A1}$$

where p,q,r are the phonon deformation potentials describing the elastic properties of the specific phonon mode of the strained crystal and, ε_{ij} are the components of the strain tensor.

The eigenvalues λ_i from Eq. (A1) are related to the Raman mode frequencies

$$\lambda_i = \omega_i^2 - \omega_0^2, \tag{A2}$$

where ω_0 and ω_i are the frequencies of unstrained and strained Ge, respectively. Since $\Delta\omega_i \ll \omega_o$, Eq. (A2) can be simplified to

$$\Delta\omega_i = \omega_i - \omega_o = \frac{\lambda_i}{2\omega_o} \tag{A3}$$

(ω_i = 1,2,3 labels the TO1, TO2, and LO mode, respectively).

Since the fins in our sample are aligned along the $\bar{1}10$, it is convenient here to work with a co-ordinate system $x'y'z'$ defined by [110], [$\bar{1}$10], and [001] crystallographic directions. Solving for a triaxial stress state with stress in only the principal directions as non-zero, i.e.,

$$\sigma_{x'x'} \neq 0,\ \sigma_{y'y'} \neq 0,\ \sigma_{z'z'} \neq 0. \tag{A4}$$

Then, the strain tensor elements ε_{ij} are related to $\sigma x'x'$, $\sigma y'y'$, and $\sigma z'z'$ by Hookes law,

$$\begin{aligned} \epsilon_{xx} = \epsilon_{yy} &= \frac{1}{2}(S_{11} + S_{12})(\sigma_{x'x'} + \sigma_{y'y'}) + S_{12}\sigma_{z'z'}, \\ \epsilon_{zz} &= S_{12}(\sigma_{x'x'} + \sigma_{y'y'}) + S_{11}\sigma_{z'z'}, \\ \epsilon_{xy} &= \frac{1}{4} S_{44}(\sigma_{x'x'} - \sigma_{y'y'}),\ \epsilon_{xz} = \epsilon_{yz} = 0, \end{aligned} \tag{A5}$$

where S_{ij} are the elastic compliance coefficients.

Considering $\epsilon_{xx} = \epsilon_{yy}$ and $\epsilon_{xz} = \epsilon_{yz} = 0$, Eq. (A1) reduces to

$$\begin{vmatrix} (p+q)\epsilon_{xx} + q(\varepsilon_{zz}) - \lambda_i & 2r\varepsilon_{xy} & 0 \\ 2r\varepsilon_{xy} & (p+q)\epsilon_{xx} + q(\varepsilon_{zz}) - \lambda_i & 0 \\ 0 & 0 & p\epsilon_{zz} + 2q\epsilon_{xx} - \lambda_i \end{vmatrix} = 0, \tag{A6}$$

with eigen vectors v_{i_st},

$$v_{1_st} = \frac{1}{\sqrt{2}}\begin{pmatrix}1\\1\\0\end{pmatrix},\ v_{2_st} = \frac{1}{\sqrt{2}}\begin{pmatrix}\bar{1}\\1\\0\end{pmatrix},\ v_{3_st} = \begin{pmatrix}0\\0\\1\end{pmatrix}, \tag{A7}$$

giving eigenvalues

$$\begin{aligned} \lambda_1 &= (p+q)\epsilon_{xx} + q\epsilon_{zz} + 2r\varepsilon_{xy}, \\ \lambda_2 &= (p+q)\epsilon_{xx} + q\epsilon_{zz} - 2r\varepsilon_{xy}, \\ \lambda_3 &= p\epsilon_{zz} + 2q\epsilon_{xx}. \end{aligned} \tag{A8}$$

Downloaded from http://pubs.aip.org/aip/jap/article-pdf/doi/10.1063/5.0100602/16510500/035104_1_online.pdf

Published under an exclusive license by AIP Publishing

Then, from Eqs. (A3), (A5), and (A8),

$$\Delta\omega_1(TO1) = \frac{1}{2\omega_0}\left[\left(\frac{1}{2}(S_{11}+S_{12})(p+q)+qS_{12}+\frac{r}{2}S_{44}\right)\sigma_{x'x'} + \left(\frac{1}{2}(S_{11}+S_{12})(p+q)+qS_{12}-\frac{r}{2}S_{44}\right)\sigma_{y'y'} + ((p+q)S_{12}+qS_{11})\sigma_{z'z'}\right], \quad \text{(A9a)}$$

$$\Delta\omega_2(TO2) = \frac{1}{2\omega_0}\left[\left(\frac{1}{2}(S_{11}+S_{12})(p+q)+qS_{12}-\frac{r}{2}S_{44}\right)\sigma_{x'x'} + \left(\frac{1}{2}(S_{11}+S_{12})(p+q)+qS_{12}+\frac{r}{2}S_{44}\right)\sigma_{y'y'} + ((p+q)S_{12}+qS_{11})\sigma_{z'z'}\right], \quad \text{(A9b)}$$

$$\Delta\omega_3(LO) = \frac{1}{2\omega_0}[(pS_{12}+q(S_{11}+S_{12}))(\sigma_{x'x'}+\sigma_{y'y'}) + (pS_{11}+2qS_{12})\sigma_{z'z'}]. \quad \text{(A9c)}$$

The detailed explanation of tensor rotations can be found elsewhere.[48]

APPENDIX B: SELECTION RULES FOR RAMAN SCATTERING INTENSITY

To identify the selection rules for each mode, we determine the strain-modified Raman tensors in the *x'y'z'* system. First, the Raman tensors for strain-perturbed phonons can be expressed as linear combinations of the tensors in Eq. (2),[23]

$$R_{i_st} = \sum_{k=1}^{3} (v_{i_st})_k R_k, \quad \text{(B1)}$$

where $(v_{i_st})_k$ denotes the *k*th component of the *i*th eigenvector v_{i_st} [Eq. (A7)],

$$R_{1_st} = \frac{1}{\sqrt{2}}\begin{pmatrix} 0 & 0 & d \\ 0 & 0 & d \\ d & d & 0 \end{pmatrix},\quad R_{2_st} = \frac{1}{\sqrt{2}}\begin{pmatrix} 0 & 0 & d \\ 0 & 0 & -d \\ d & -d & 0 \end{pmatrix},\quad R_{3_st} = \begin{pmatrix} 0 & d & 0 \\ d & 0 & 0 \\ 0 & 0 & 0 \end{pmatrix}. \quad \text{(B2)}$$

While measuring, the finFET sample is oriented in such a way that $E_{in||} = [\bar{1}10]$ and $E_{in\perp} = [001]$. Under this orientation, the "strained tensors" R_{i_st} in Eq. (B2), must be rotated by 45° about the [001] axis to determine the selection rules,[18]

$$R'_{i_st} = A(45^\circ).R_{i_st}.A(45^\circ)^T. \quad \text{(B3)}$$

With *A* as the Euler rotation matrix

$$A(45^\circ) = \frac{1}{\sqrt{2}}\begin{pmatrix} 1 & 1 & 0 \\ -1 & 1 & 0 \\ 0 & 0 & \sqrt{2} \end{pmatrix}, \quad \text{(B4)}$$

$$R'_{1_st}(TO1) = \begin{pmatrix} 0 & 0 & d \\ 0 & 0 & 0 \\ d & 0 & 0 \end{pmatrix},\quad R'_{2_st}(TO2) = \begin{pmatrix} 0 & 0 & 0 \\ 0 & 0 & -d \\ 0 & -d & 0 \end{pmatrix},\quad R'_{3_st}(LO) = \begin{pmatrix} d & 0 & 0 \\ 0 & -d & 0 \\ 0 & 0 & 0 \end{pmatrix}. \quad \text{(B5)}$$

The selection rules from Eq. (B5) are summarized in Table I. E_{in} is fixed while a polarization analyzer is used to select specific E_{out} polarizations and isolate the different phonon modes.

REFERENCES

[1] C.-F. Lee, R.-Y. He, K.-T. Chen, S.-Y. Cheng, and S.-T. Chang, Microelectron. Eng. **138**, 12 (2015).
[2] K. Usuda, T. Numata, and S. Takagi, Mater. Sci. Semiconductor Processing **8**(1–3), 155–159 (2005).
[3] M. J. Hÿtch, E. Snoeck, and R. Kilaas, Ultramicroscopy **74**, 131 (1998).
[4] J.-L. Rouviere, A. Béché, Y. Martin, T. Denneulin, and D. Cooper, Appl. Phys. Lett. **103**, 241913 (2013).
[5] Z. Ma and D. G. Seiler, *Metrology and Diagnostic Techniques for Nanoelectronics* (Jenny Stanford Publishing, 2017).
[6] A. Schulze, T. Loo, P. Ryan, M. Wormington, P. Favia, L. Witters, N. Collaert, H. Bender, W. Vandervorst, and M. Caymax, Nanotechnology **28**, 145703 (2017).
[7] S. Ganesan, A. A. Maradudin, and J. Oitmaa, Ann. Phys. **56**, 556 (1970).
[8] G. H. Loechelt, N. G. Cave, and J. Menéndez, Appl. Phys. Lett. **66**, 3639 (1995).
[9] I. De Wolf, H. E. Maes, and S. K. Jones, J. Appl. Phys. **79**, 7148 (1996).
[10] R. Loudon, Adv. Phys. **13**, 423 (1964).
[11] F. Cerdeira, C. J. Buchenauer, F. H. Pollak, and M. Cardona, Phys. Rev. B **5**, 580 (1972).
[12] R. Ossikovski, Q. Nguyen, G. Picardi, J. Schreiber, and P. Morin, J. Raman Spectrosc. **39**, 661 (2008).
[13] D. Kosemura and A. Ogura, Jpn. J. Appl. Phys. **50**, 04DA06 (2011).
[14] D. Kosemura and A. Ogura, Appl. Phys. Lett. **96**, 212106 (2010).
[15] V. Prabhakara, T. Nuytten, H. Bender, W. Vandervorst, S. Bals, and J. Verbeeck, Opt. Express **29**, 34531 (2021).
[16] T. Nuytten, J. Bogdanowicz, L. Witters, G. Eneman, T. Hantschel, A. Schulze, P. Favia, H. Bender, I. De Wolf, and W. Vandervorst, APL Mater. **6**, 058501 (2018).
[17] D. Kosemura, M. Tomita, K. Usuda, and A. Ogura, "Stress measurements in Si and SiGe by liquid-immersion Raman spectroscopy," in *Advanced Aspects of Spectroscopy* (InTech, 2012).
[18] R. Ossikovski, Q. Nguyen, G. Picardi, and J. Schreiber, J. Appl. Phys. **103**, 093525 (2008).

Downloaded from http://pubs.aip.org/aip/jap/article-pdf/doi/10.1063/5.0100602/16510500/035104_1_online.pdf

Published under an exclusive license by AIP Publishing

[19]G. Ndong, G. Picardi, C. Licitra, D. Rouchon, J. Eymery, and R. Ossikovski, J. Appl. Phys. **114**, 164309 (2013).
[20]E. Anastassakis and Y. S. Raptis, J. Appl. Phys. **57**, 920 (1985).
[21]N. A. Macleod, A. Goodship, A. W. Parker, and P. Matousek, Anal. Chem. **80**, 8146 (2008).
[22]J. W. Kang, Y. S. Park, H. Chang, W. Lee, S. P. Singh, W. Choi, L. H. Galindo, R. R. Dasari, S. H. Nam, J. Park, and P. T. C. So, Sci. Adv. **6**, eaay5206 (2020).
[23]G. H. Loechelt, N. G. Cave, and J. Menéndez, J. Appl. Phys. **86**, 6164 (1999).
[24]K. F. Dombrowski, I. De Wolf, and B. Dietrich, Appl. Phys. Lett. **75**, 2450 (1999).
[25]P. Favia, M. Bargallo Gonzales, E. Simoen, P. Verheyen, D. Klenov, and H. Bender, J. Electrochem. Soc. **158**, H438 (2011).
[26]D. A. Long, *The Raman Effect: A Unified Treatment of the Theory of Raman Scattering by Molecules* (Wiley, Chichester, 2002), Vol. 8.
[27]S. Yamamoto, D. Kosemura, S. N. C.M.Yusoff, T. Kijima, R. Imai, K. Takeuchi, R. Yokogawa, K. Usuda, and A. Ogura, ECS Meet. Abstr. **MA2014-02**, 1848 (2014).
[28]D. Kosemura, S. N. B. Che Mohd Yusoff, and A. Ogura, J. Raman Spectrosc. **45**, 414 (2014).
[29]A. Lucia, O. A. Cacioppo, E. Iulianella, L. Latessa, G. Moccia, D. Passeri, and M. Rossi, Appl. Phys. Lett. **110**, 103105 (2017).
[30]G. M. Vanacore, M. Chaigneau, N. Barrett, M. Bollani, F. Boioli, M. Salvalaglio, F. Montalenti, N. Manini, L. Caramella, P. Biagioni, D. Chrastina, G. Isella, O. Renault, M. Zani, R. Sordan, G. Onida, R. Ossikovski, H. J. Drouhin, and A. Tagliaferri, Phys. Rev. B **88**, 115309 (2013).
[31]P. Hermann, M. Hecker, D. Chumakov, M. Weisheit, J. Rinderknecht, A. Shelaev, P. Dorozhkin, and L. M. Eng, Ultramicroscopy **111**, 1630 (2011).
[32]H. Wen, Y. Ji, and B. Jalali, IEEE Photonics J. **8**(5), 1–12, 2600412.
[33]J. Bogdanowicz, T. Nuytten, A. Gawlik, A. Schulze, I. De Wolf, and W. Vandervorst, Appl. Phys. Lett. **108**, 083106 (2016).
[34]T. Nuytten, J. Bogdanowicz, T. Hantschel, A. Schulze, P. Favia, H. Bender, I. De Wolf, and W. Vandervorst, Adv. Eng. Mater. **19**, 1600612 (2017).
[35]A. Gawlik, J. Bogdanowicz, A. Schulze, T. Nuytten, K. Tarnowski, J. Misiewicz, and W. Vandervorst, Appl. Phys. Lett. **113**, 063103 (2018).
[36]A. Gawlik, J. Bogdanowicz, T. Nuytten, A.-L. Charley, L. Teugels, J. Misiewicz, and W. Vandervorst, Appl. Phys. Lett. **117**, 043102 (2020).
[37]R. Loo, L. Souriau, P. Ong, K. Kenis, J. Rip, P. Storck, T. Buschhardt, and M. Vorderwestner, J. Cryst. Growth **324**, 15 (2011).
[38]B. Vincent, L. Witters, O. Richard, A. Hikavyy, H. Bender, R. Loo, M. Caymax, and A. Thean, ECS Trans. **50**, 39 (2013).
[39]J. Mitard, L. Witters, R. Loo, S. H. Lee, J. W. Sun, J. Franco, L. Ragnarsson, A. Brand, X. Lu, N. Yoshida, G. Eneman, D. P. Brunco, M. Vorderwestner, P. Storck, A. P. Milenin, A. Hikavyy, N. Waldron, P. Favia, D. Vanhaeren, A. Vanderheyden, R. Olivier, H. Mertens, H. Arimura, S. Sonja, C. Vrancken, H. Bender, P. Eyben, K. Barla, S. G. Lee, N. Horiguchi, N. Collaert, and A. V. Y. Thean, "15nm-WFIN high-performance low-defectivity strained-germanium pFinFETs with low temperature STI-last process," in *2014 Symposium on VLSI Technology (VLSI-Technology): Digest of Technical Papers* (2014), pp. 1–2.
[40]S. C. Jain, B. Dietrich, H. Richter, A. Atkinson, and A. H. Harker, Phys. Rev. B **52**, 6247 (1995).
[41]W. A. Brantley, J. Appl. Phys. **44**, 534 (1973).
[42]D. E. Aspnes and A. A. Studna, Phys. Rev. B **27**, 985 (1983).
[43]V. I. Korepanov and D. M. Sedlovets, Analyst **143**, 2674 (2018).
[44]J. Wolberg, *Data Analysis Using the Method of Least Squares: Extracting the Most Information From Experiments* (Springer Science & Business Media, 2006).
[45]S. Palleschi, D. Mastrippolito, P. Benassi, M. Nardone, and L. Ottaviano, Appl. Surf. Sci. **561**, 149691 (2021).
[46]D. Mastrippolito, S. Palleschi, S. Tosti, and L. Ottaviano, Appl. Surf. Sci. **567**, 150824 (2021).
[47]R. Jalilian, G. U. Sumanasekera, H. Chandrasekharan, and M. K. Sunkara, Phys. Rev. B **74**, 155421 (2006).
[48]I. De Wolf, J. Appl. Phys. **118**, 053101 (2015).

Downloaded from http://pubs.aip.org/aip/jap/article-pdf/doi/10.1063/5.0100602/16510500/035104_1_online.pdf

Published under an exclusive license by AIP Publishing